

Neuron

Supplemental Information

Environmental Boundaries

as an Error Correction

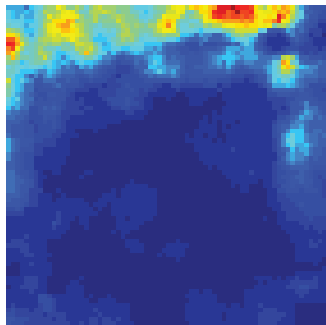
Mechanism for Grid Cells

Kiah Hardcastle, Surya Ganguli, and Lisa M. Giocomo

Figure S1

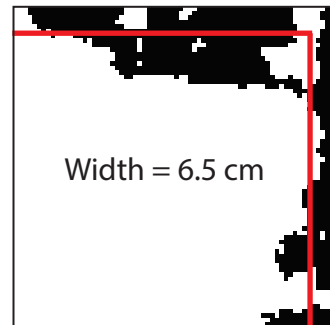
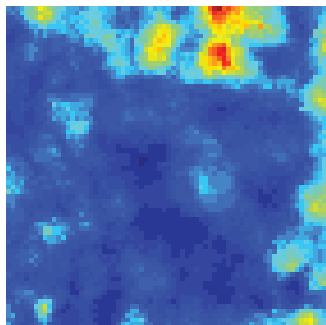
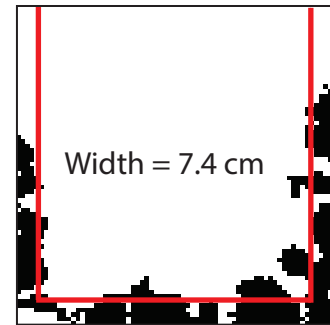
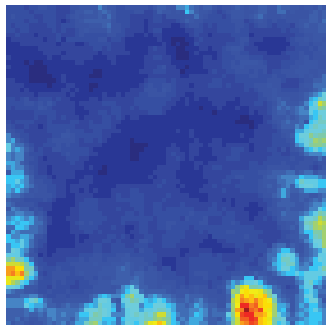
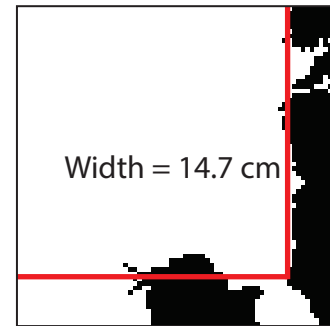
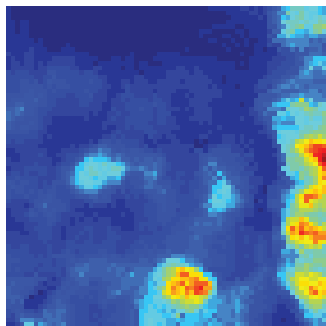
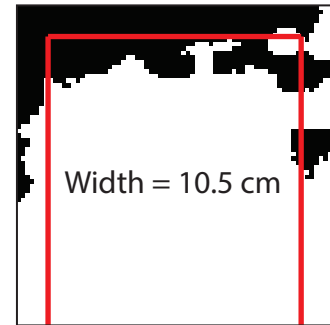
A

Firing rate map

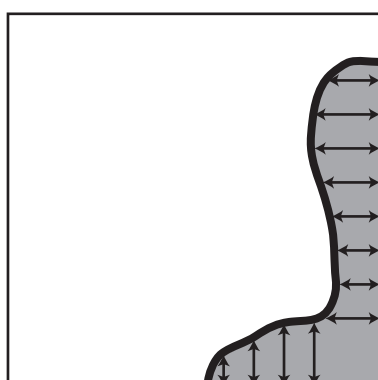


B

Firing field



C



D

Mean = 11 cm

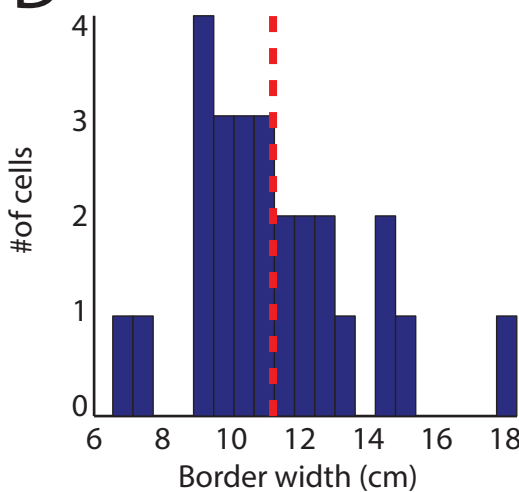
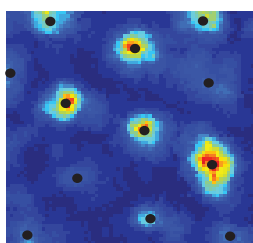
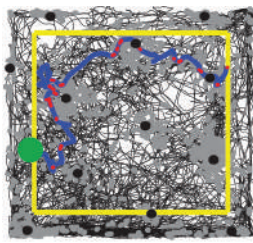
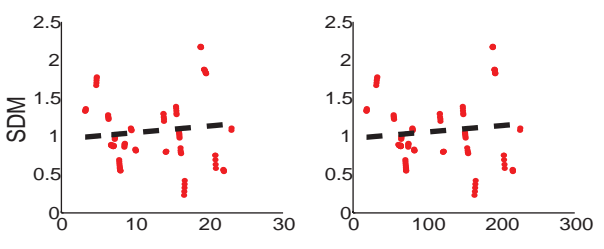
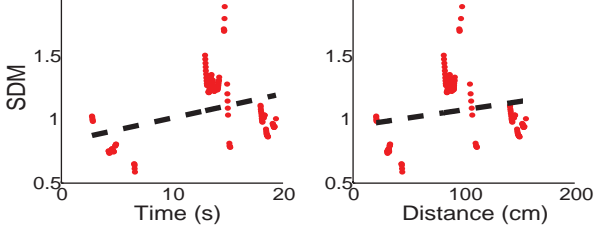
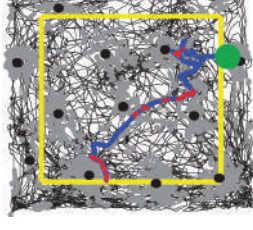
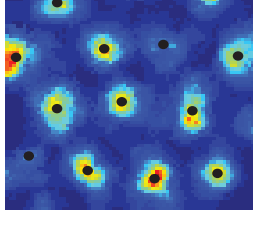
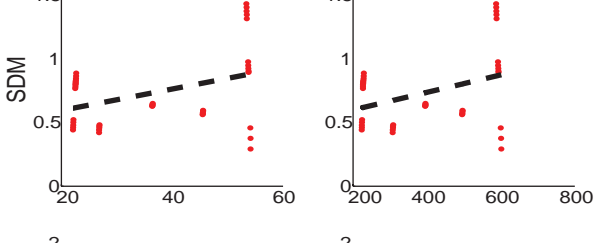
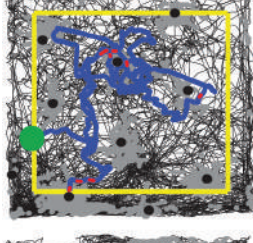
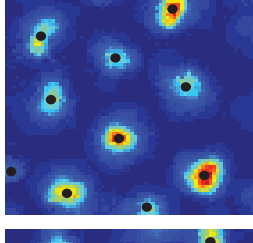
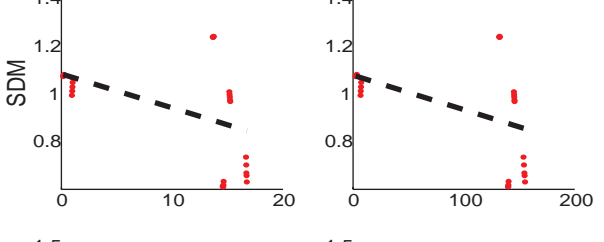
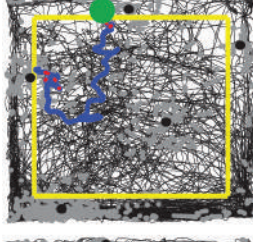
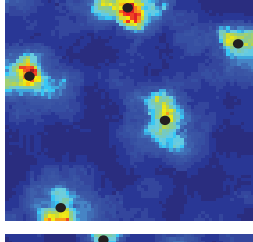
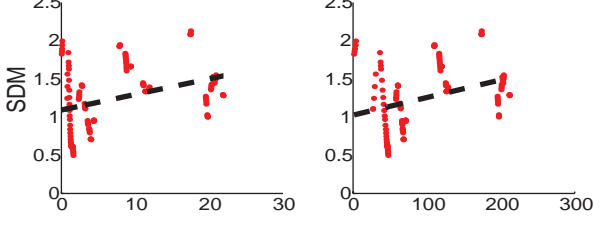
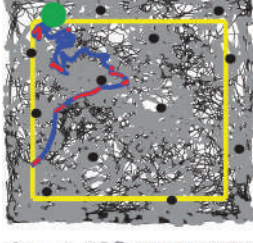
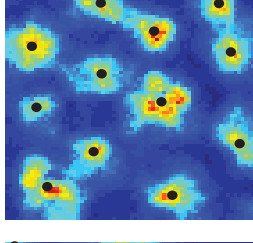
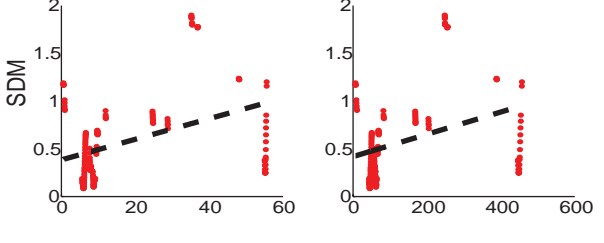
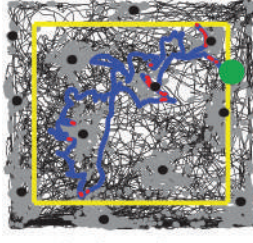
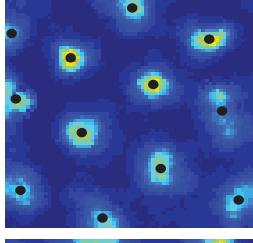
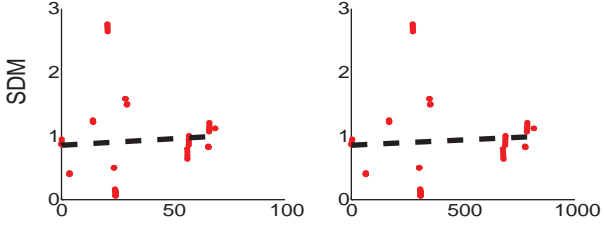
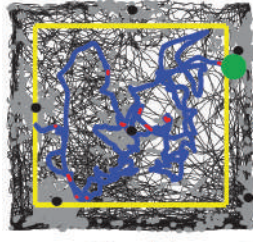
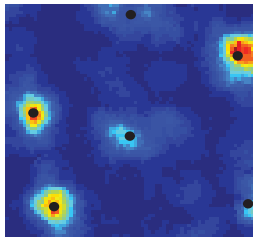
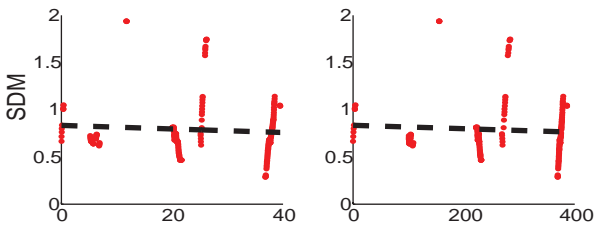
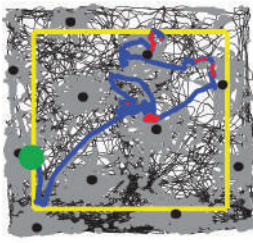
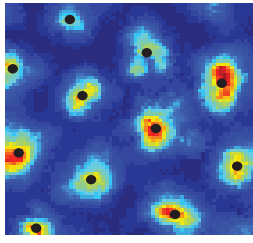
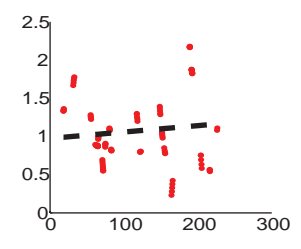


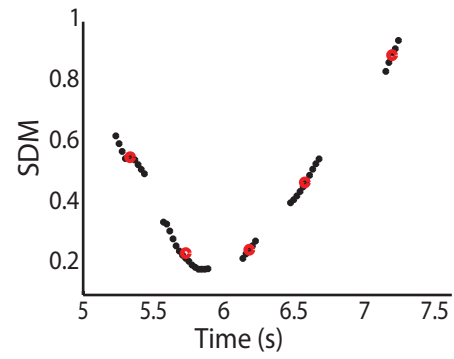
Figure S2

A**B****C****D**

Time (s) Distance (cm)

Figure S3

A

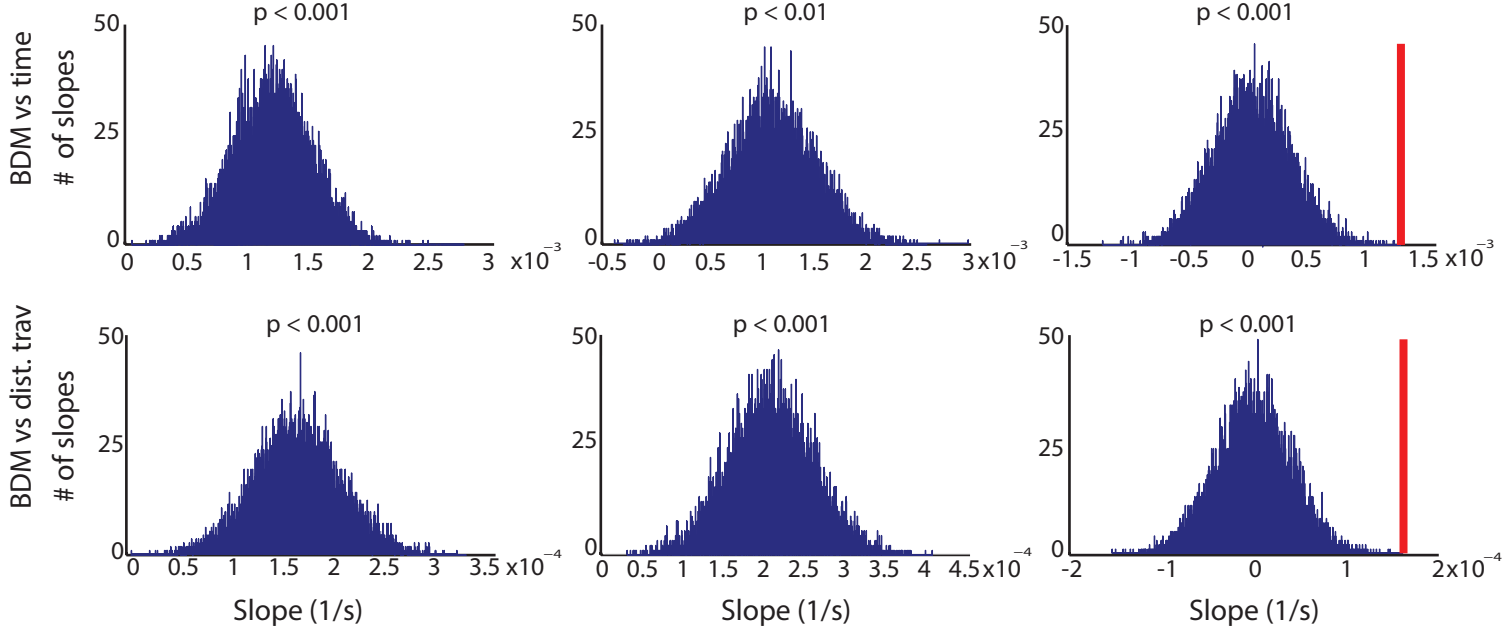


B

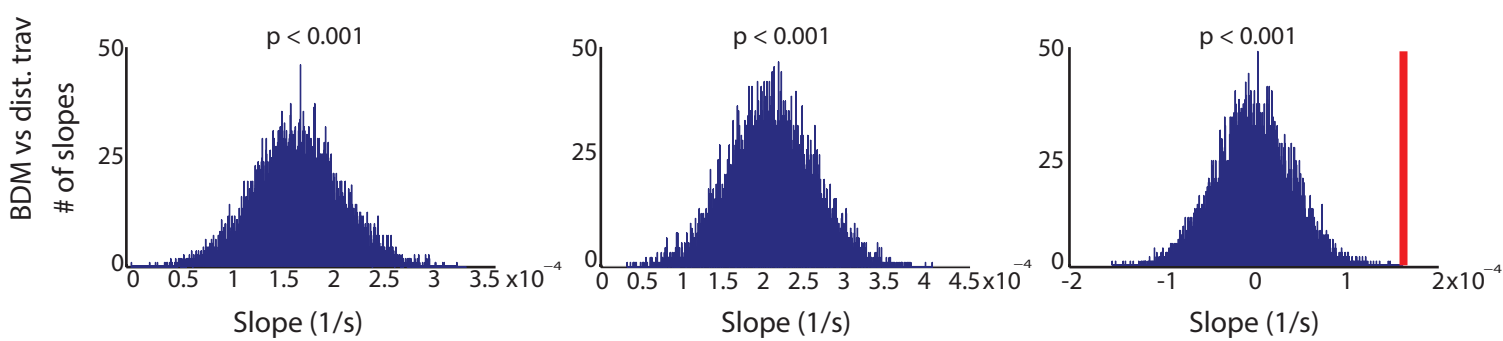
Bootstrapping

Downsampling

Shuffling



C



D

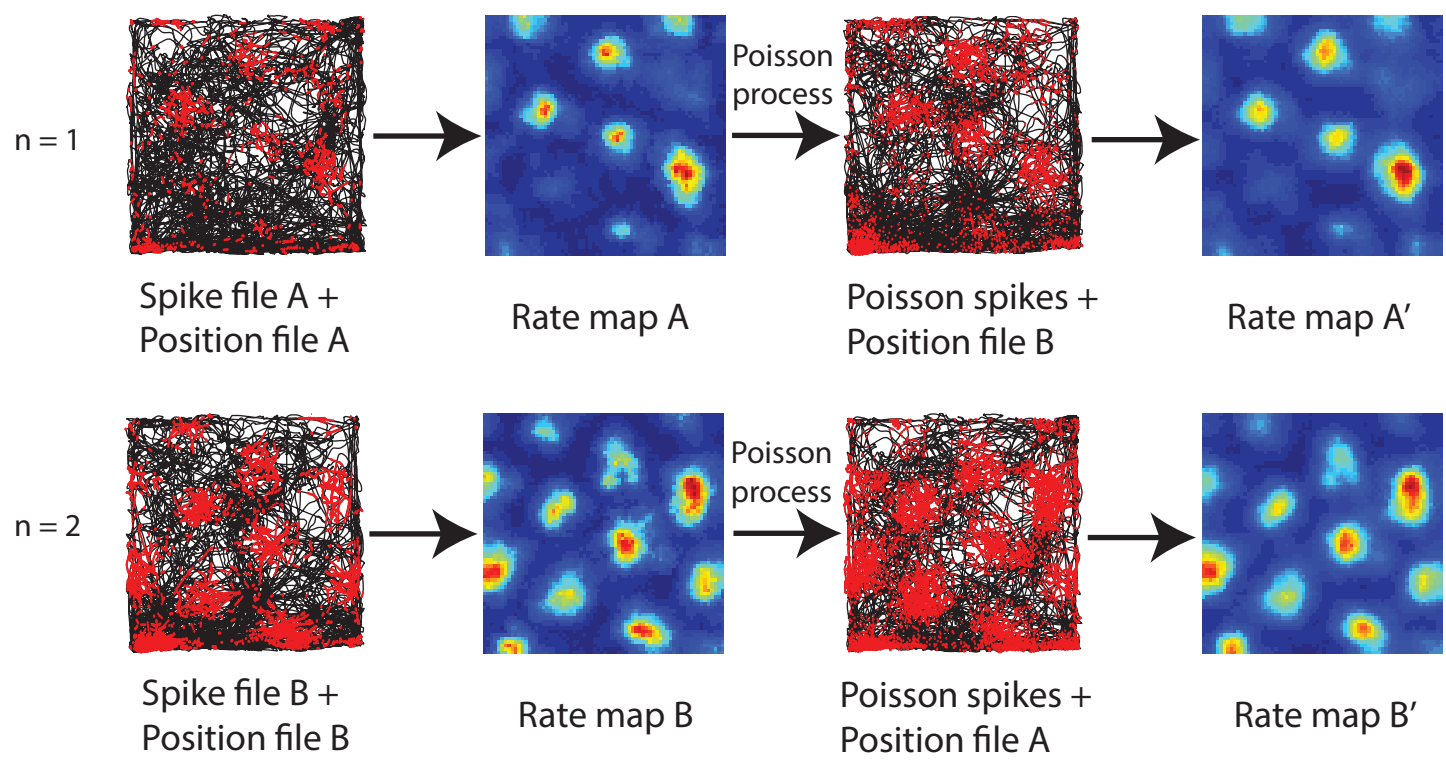
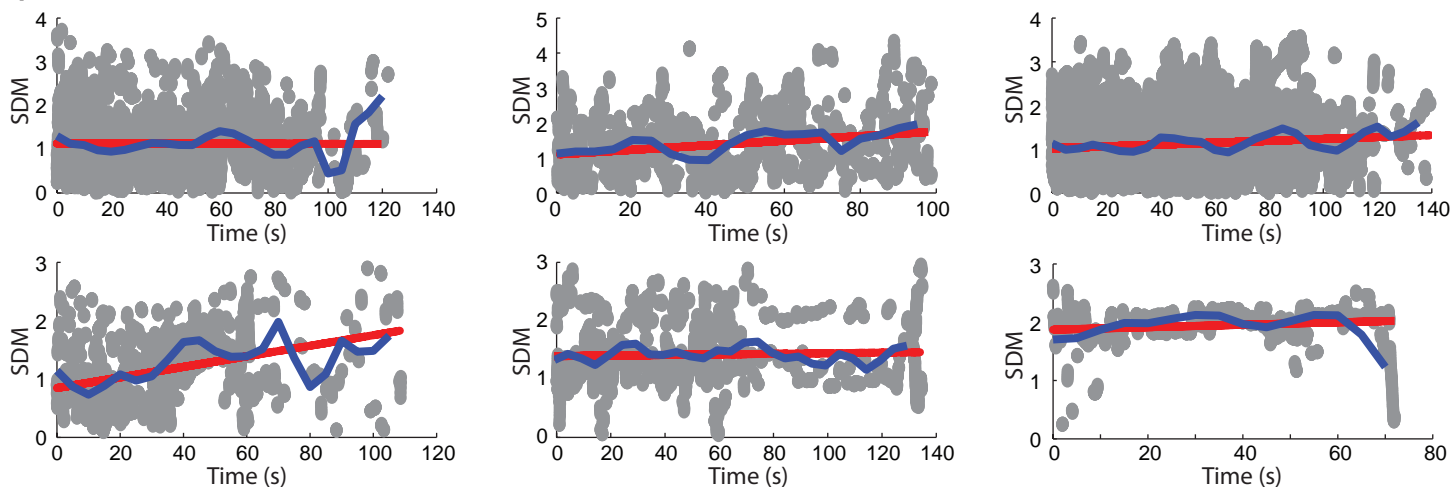
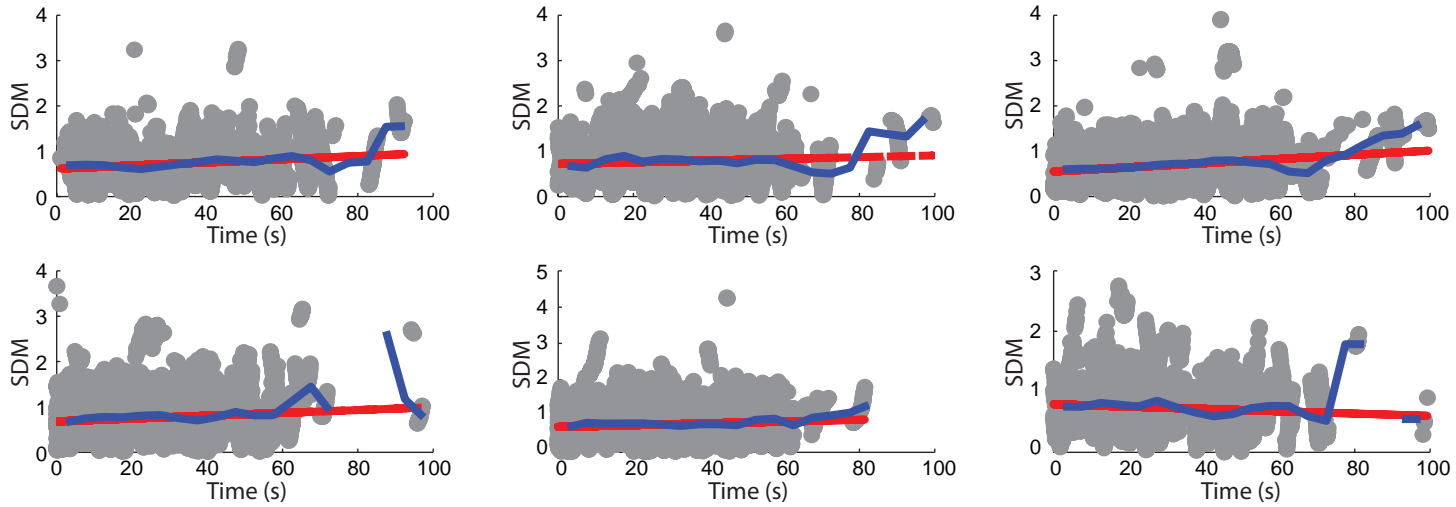


Figure S4

A Experimental Data



B Computational Simulations



C

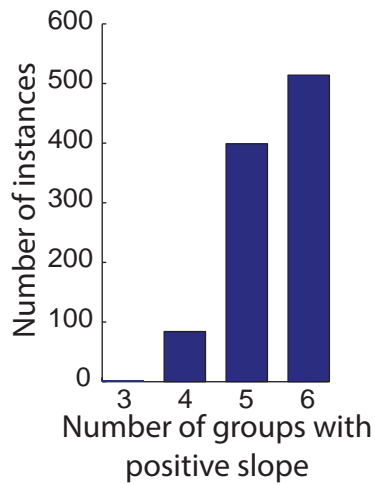


Figure S5

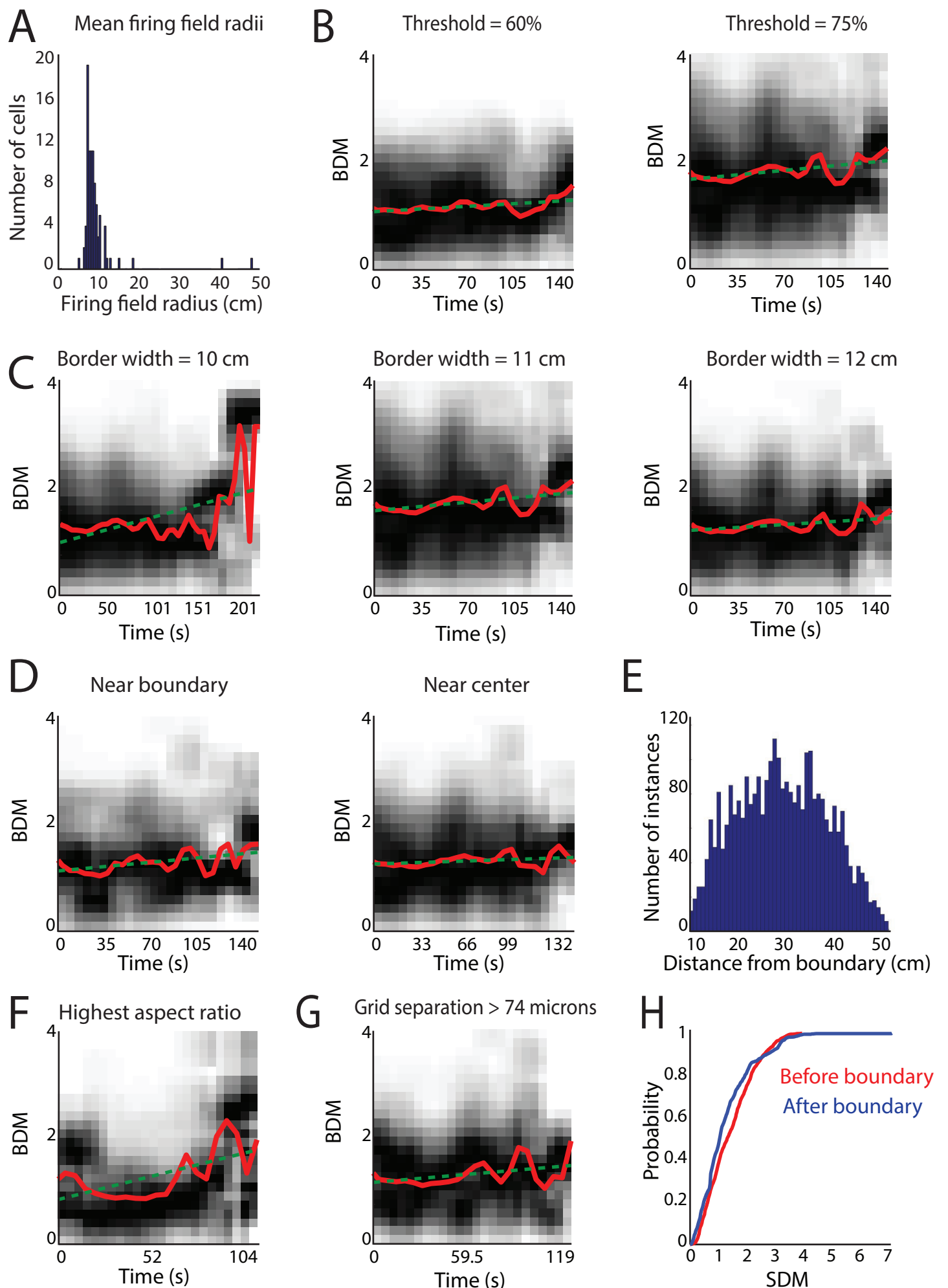


Figure S6

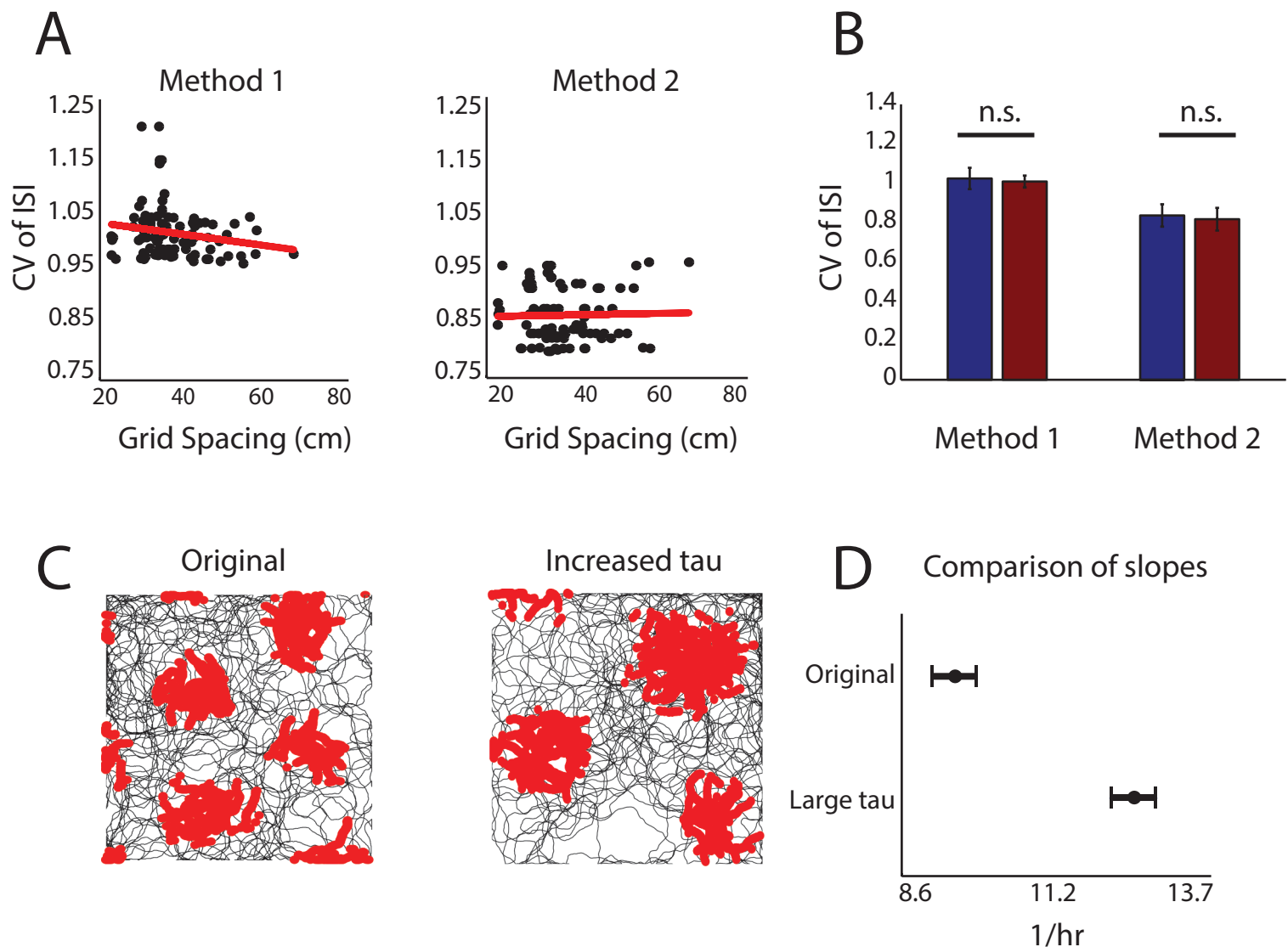
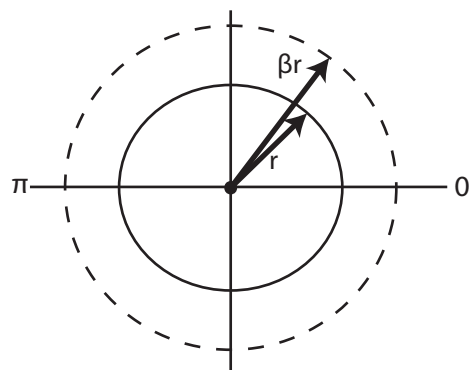
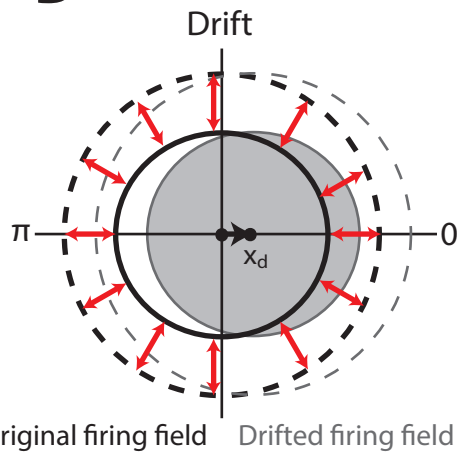


Figure S7

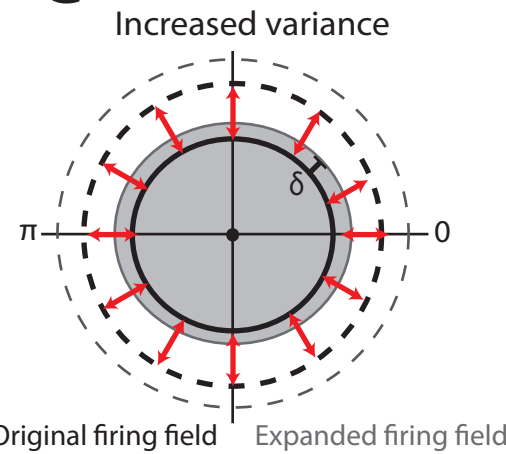
A



B

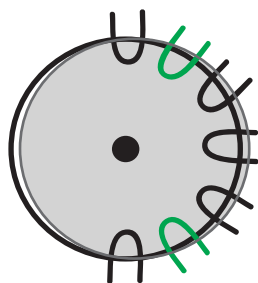


C

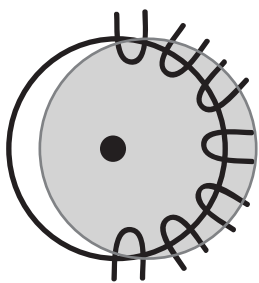


D

Angle of entry-exit = 10 degrees



Average $\alpha\beta = .43$

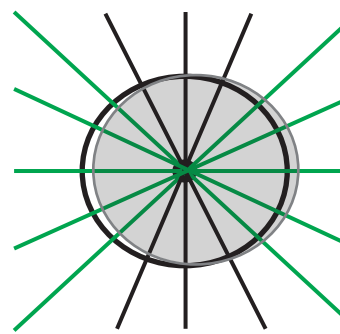


Average $\alpha\beta = 1$

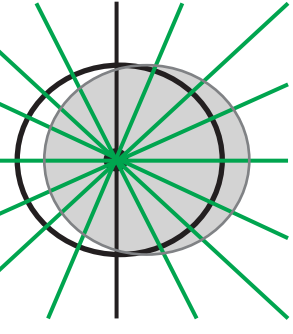
E

Angle of entry-exit = 180 degrees

- $\alpha\beta = -1$
- $\alpha\beta = 1$



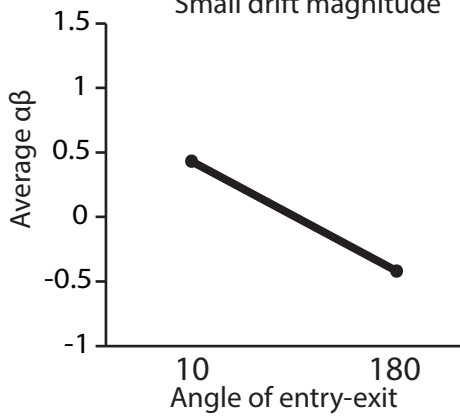
Average $\alpha\beta = -.43$



Average $\alpha\beta = -.71$

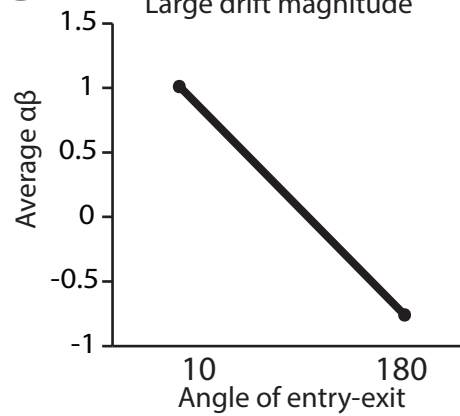
F

Small drift magnitude

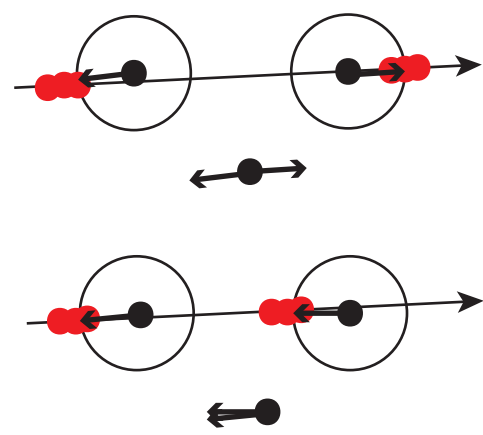


G

Large drift magnitude



H



I

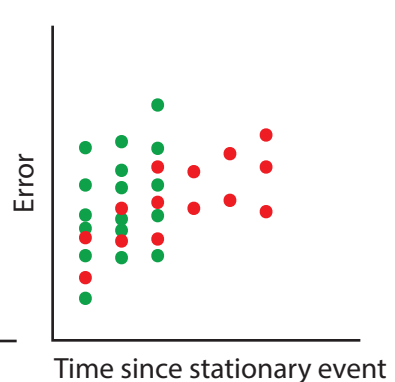
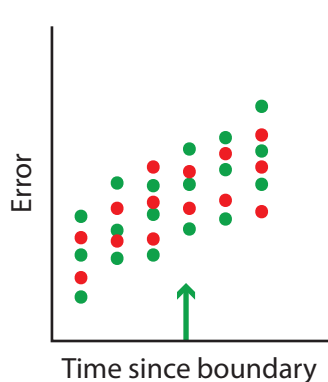
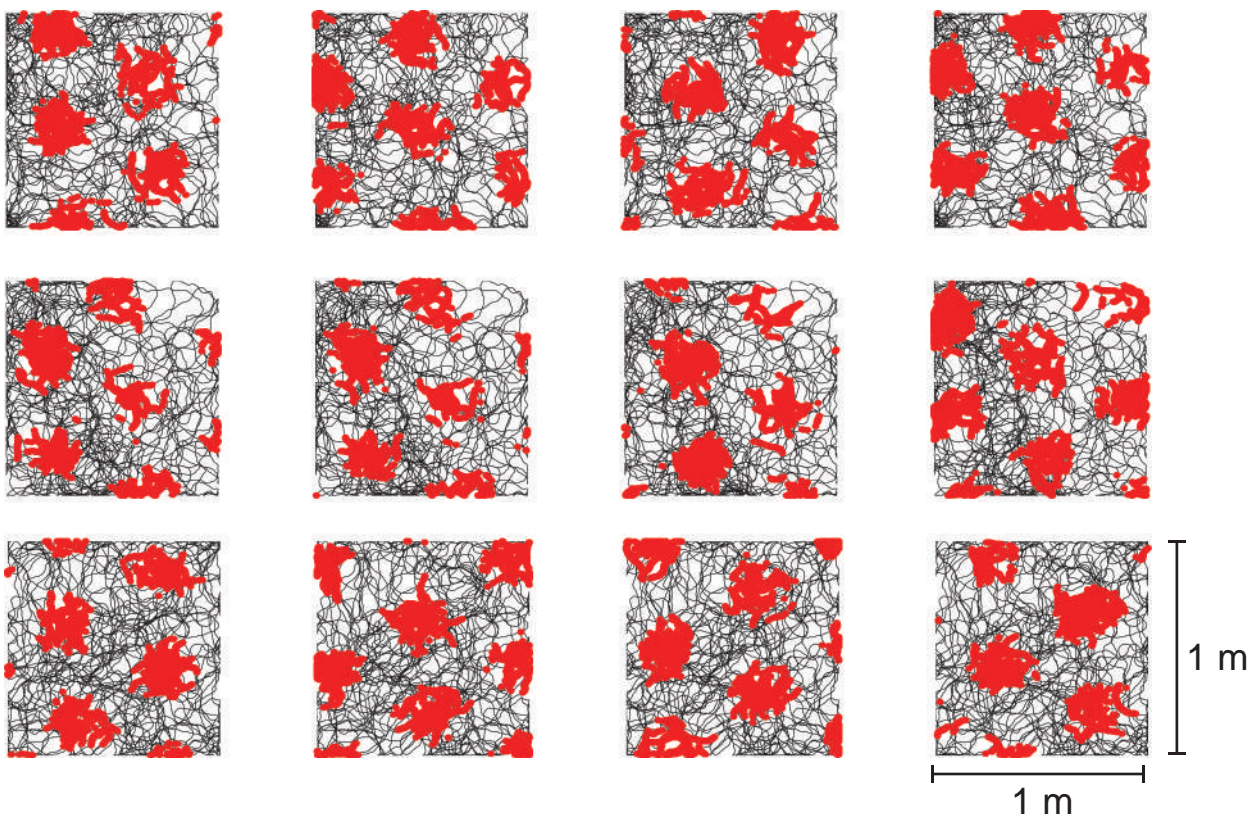
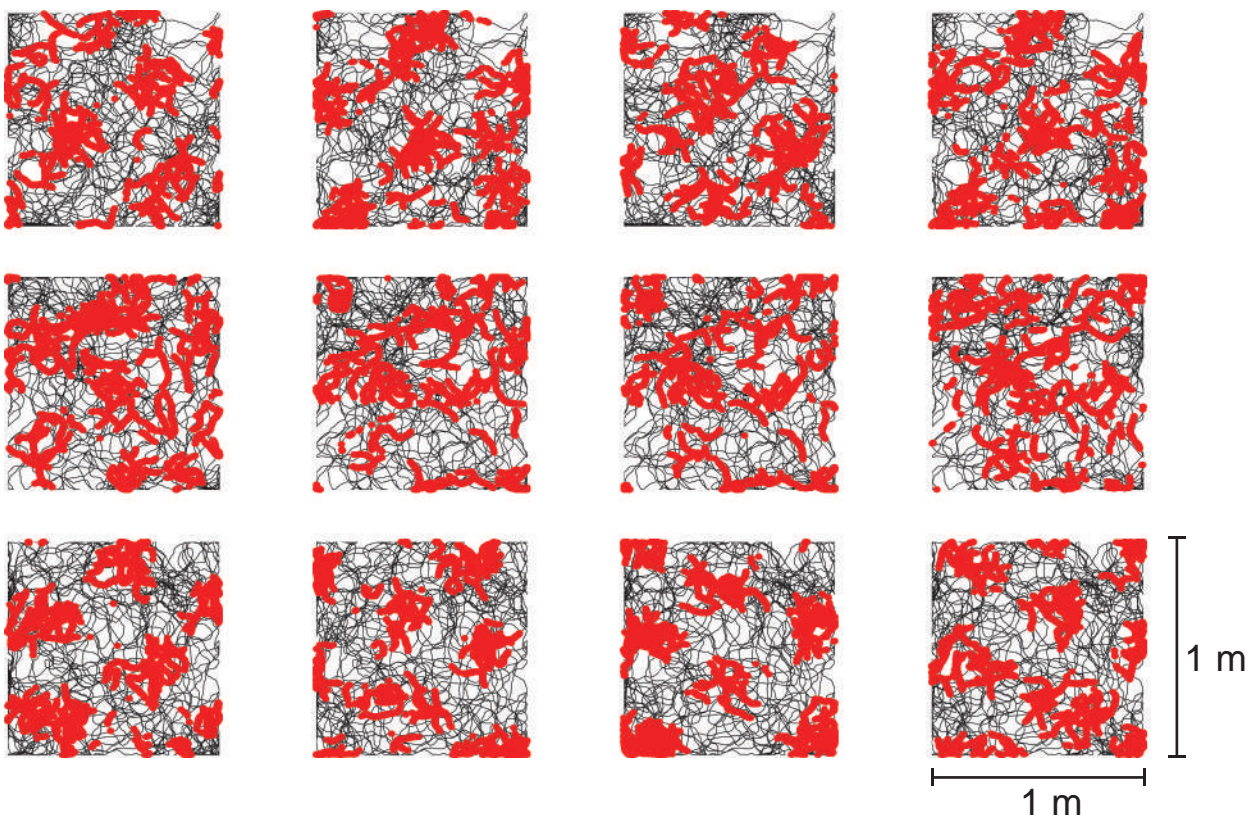


Figure S8

With border cell input:



Without border cell input:



Supplemental Figure Legends

Figure S1, related to Figure 1 and Figure 6. Example border cells and calculation of border width

(A)-(B). Four representative border cells. The left panels give the firing rate maps of each example border cell, color-coded to show minimum (blue) and maximum (red) firing rate values. The right panels give the firing fields detected in the corresponding rate map (black), with a red line depicting the mean maximal distance of the firing fields from the boundary. The mean width for each border cell is given in the center of each panel. (C) Schematic of how we calculated the mean maximal firing field distance from the border. After identifying firing fields (illustrated in gray), we then identified the edge of the firing field (denoted by thick black line) by identifying the bins that neighbor non-field bins. For each bin along this edge, we then calculated the distance from each bin to the nearest E/W and N/S wall. For each bin, we recorded the minimal distance (the distance to the nearest wall and denoted in the figure by the arrows). The mean firing field width for each firing field is the mean of these values. For each cell, we then calculated the mean width over all firing fields. (D) A histogram of the mean maximal firing field distance from the nearest environmental boundary for each border cell, with the mean value (11 cm) overlaid in red.

Figure S2, related to Figure 1. Examples of representative trajectories from different grid cells

(A) Firing rate maps for each cell. Eight different grid cells are shown. Maps are color-coded to show minimum (blue) and maximum (red) firing rate values. The COM of each firing field is given by a black dot in the center of the field. (B) Example trajectories (blue) with spikes overlaid (red) as the animal navigates from and to the boundary region (outlined in yellow, start of trajectory given by green dot). Grid cell spikes recorded over the course of the entire session

are given in gray, and the black line denotes the trajectory of the animal during the session. As in panel A, COMs are marked in black. (C)-(D) SDM for each spike (red) along the trajectory for time (C) and distance traveled (D) from boundary region exit to entry, with a black dashed line given by a first-order polynomial fit using the ordinary least-squares method overlaid. Note that not all trajectories exhibited an increasing SDM over time and distance traveled, as some trajectories traversed only a few firing fields, and at unequal distances from the center of mass.

Figure S3, related to Figure 1. Burst detection, statistical tests applied to BDM and generation of the null model

(A) Example of spike burst detection. The black dots correspond to spikes, while the red dots mark the center of mass of each spike train. (B)-(C) Results from statistical tests applied to BDM for trajectories > 60 s across time and distance traveled. For each bootstrapping test, BDM values were resampled with replacement and fit with a first-order polynomial using the method of ordinary least squares. This procedure was carried out 10,000 times, and the resulting slopes are plotted in the histograms shown in the leftmost column. The p-value given above each plot was derived from the proportion of the distribution less than or equal to 0. For each down-sampling test, the x-axis (time or distance traveled) was binned, where the number of bins chosen is the maximum number of bins for which at least 10% of the data is contained in each bin. The mean value in each bin was then calculated and used to fit a line (as in the bootstrapping method). This procedure was carried out 10,000 times, and a p-value was derived from the proportion of slopes less than 0. For each shuffling test, the error values were randomly shuffled along the time or distance traveled axis, and as previously described, a line was fit to the resulting values. This procedure was also carried out 10,000 times, and a p-value was derived from the overlap from the slope calculated from the unshuffled data and the distribution of slopes calculated from the shuffled data. (D) Schematic of generation of null

model. For each cell, a rate map was generated from the position and spike files. For the first null cell ($n=1$), spike file A and position file A generate rate map A. We then pseudo-randomly draw a new position file from a different recording session (in this case, the position file from cell B), and use this new position file in combination with Poisson spiking to generate a new spike file, and thus a new rate map (rate map A'; described for clarity here but not used in the simulations). We then use position file B and the Poisson spikes to determine spike distances from the nearest COM (determined from rate map A) during boundary-to-boundary trajectories. This process is carried out for every cell, allowing us to generate an entirely new, non-error accumulating data set.

Figure S4, related to Figure 1. Error accumulation in individual animals

(A) Scatter plots for individual animals that had at least two cells with at least one trajectory > 60 s. 5 of the 6 animals exhibit significant error accumulation when considering the bootstrapping and shuffling tests (with the exception of the top left animal, error accumulation bootstrapping and shuffling $p < 0.03$). 4 of the 6 animals exhibit significant error accumulation when considering the downsampling test (with the exception of the top left and bottom middle animals, downsampling $p < 0.001$). By extending the null dataset framework to create animal datasets that do not exhibit error accumulation, we find that the probability of seeing significance in all 3 tests in 4/6 animals is $p = 0.029$ and the probability of seeing significance in 2 of the tests in 5/6 animals is $p = 0.010$ (see Null Animal Dataset in Supplemental Experimental Procedures). **(B)** We compared the previous experimental result with the analogous analyses applied to the simulated data generated from the attractor network mode to generate predictions regarding what one might expect to see when sub-sampling data points (simulated cell $n = 50$). Scatter plots shown for different groups of cells. Each group of cells represents simulated animal data. Note that although the model grid cell network is drifting over time, 5 of the 6 animals exhibit

error accumulation. (C) As the number of groups of cells that exhibit significant error accumulation will vary when randomly sampling across cells, we also generated a histogram of the number of animals that exhibit a positive slope when randomly grouping 50 cells into 6 animals. Note that detection of positive error accumulation across all animals does not always occur.

Figure S5, related to Figure 3. BDM versus time for varied field-detection thresholds, border widths, field asymmetry, and anatomically separated grid cells

(A) Mean firing field radii for all cells. Two cells with large radii (> 20 cm, 2/91) are likely falsely detected grid cells by the grid score metric. Including these cells, the mean firing field radius is 9 cm; without these cells, the mean firing field radius is 8.3 cm. (B) BDM versus time since the last boundary touch with a field detection threshold of 60% (left) and 75% (right, default value). This threshold set the minimum firing rate threshold for a bin to be considered as part of a firing field. In both cases, statistical analyses by bootstrapping, down-sampling, and shuffling yielded a positive slope with $p < 0.001$. This result suggests that the BDM increase over time is not due to a failure to identify firing fields, but instead reflects error accumulation in the grid cell code. (C) BDM versus time since the boundary touch with a boundary region width of 10 cm (left), 11 cm (middle, default value), and 12 cm (right). The long trajectories that occur when considering a 10 cm boundary region width arise from a single recording session (with several simultaneously recorded grid cells), during which the animal reaches exactly 11 cm from the boundary and then loops back out into the environment. In all cases, statistical analyses by bootstrapping, downsampling, and shuffling yielded a positive slope with $p < 0.05$. These results show that error accumulation was not an effect of our choice of parameters, but instead is a robust result that persists with perturbation to our field-detection and border-width parameters. (D) BDM versus time is significant when considering spike bursts that occur when the animal is near the

center of the box (> 22 cm away; twice the boundary region width) and close to the boundary (between 11 and 22 cm away) (bootstrapping, downsampling, shuffling $p < 0.05$; Near the boundary slope = 0.0010; Near the center slope = 0.0014; Comparison of slopes $F(1,6111) = 0.26$ and $p = 0.61$). (E) A histogram of the distance at which the top 50% of the BDM values occur. Note that all distances from the boundary contain high BDM values. (F) A circularity score for each field was calculated as the aspect ratio (ratio between the major and minor axes) of the best-fit ellipse. We considered spikes associated with fields above a circularity score of 0.9 (most circular fields) and found that BDM significantly increases over time (bootstrapping, shuffling and downsampling yield a positive slope with $p < 0.001$; slope = 0.0030) for trajectories > 60 s. (G) BDM versus time increases when considering cells separated by at least 75 microns (bootstrapping, shuffling, and downsampling $p < 0.01$). We based this value off of published guidelines for cell separation in rats. Isolated units were treated as unique if the tetrode was moved > 60 microns from the previous session (Wilber et al., 2014). (H) To directly investigate whether error accumulates during the entire session or if error decreases after a boundary encounter, we investigated the SDM values in the 5 seconds before and after an animal traversed the boundary region line (11 cm from the environmental walls) for trajectories > 60 s. We found that the SDM values immediately prior to a boundary encounter were larger than the SDM values immediately after a boundary encounter (spike before $n = 3,089$, spike after $n = 3,248$; median SDM before = 1.30, median SDM after = 1.05, WRS test: $z = 9.15$, $p < 0.001$). This effect is shown in the cumulative distribution plot by a leftward shift of the cumulative distribution of SDM values observed after boundary encounters. The SDM distributions were significantly different (KS test: $K = 0.13$, $p < 0.001$). This result provides additional evidence that boundaries correct accumulated error and that the error accumulation we observe does not reflect error accumulated over the entire session but rather error accumulated relative to the time and distance traveled since the last boundary encounter.

Figure S6, related to Figure 3. Mechanisms of grid error accumulation across grid scales

(A) Calculation of stochasticity of firing, as measured by the coefficient of variation (CV) for the inter-spike interval (ISI) across grid cells with varied grid spacing. As the calculation of $CV = \text{std}(ISI)/\text{mean}(ISI)$ assumes a constant mean firing rate, we calculated CV by identifying two types of intervals with constant firing rate, as in Burak & Fiete, 2009. In the first method, we considered low-speed intervals in which the mouse was moving below a certain speed (5 cm/s) for at least 1 second, and where the grid cell fired at least 3 spikes (from which 2 ISI intervals could be detected). We removed intervals where the animal moved more than 10 cm, increasing the possibility that the animal was likely to be either located inside or outside a grid field for the entire duration of the interval. In the second method, we considered intervals when the mean firing rate of the grid was above 10 Hz for at least 1 second, suggesting that the animal was physically located within a firing field. In the first method (left), the CV exhibits a non-significant negative correlation with grid scale (Pearson's rho = -0.18, p = 0.08), while the second method (right) yields a non-significant positive correlation with grid scale (Pearson's rho = 0.03, p = 0.81). Each point is associated with the mean CV and grid scale of one grid cell. (B) To investigate the CV for cells grouped according to scale as in Figure 2F (small-scaled cells had spacing < 35 cm, large-scaled cells had spacing > 35 cm), we compared the mean CV as calculated by method 1 (left) and method 2 (right) for each group (blue = small-scale grid cells, red = large-scale grid cells). In both cases, large-scale grid cells exhibit a non-significant decrease in CV (method 1 yields p = 0.11, method 2 yields p = 0.17 by Student's t-test). Error bars correspond to standard error of the mean. (C) Increasing the time-constant of neural integration (τ) increases grid scale in the attractor network model presented in this work. Single neuron output of a simulation with $\tau = 30$ ms is shown on the left, while single neuron output of a simulation with $\tau = 35$ ms is shown on the right. (D) Using the methods presented to calculate the slope of the SDM over time for long trajectories in the simulated data, we find that the slope of the SDM versus time is significantly higher for cells with increased τ (ANCOVA F(1,203744) =

53.49, $p < 0.001$), suggesting that cells with increased τ exhibit increased error. The error bars are generated through calculating uncertainty intervals based on (Hochberg and Tamhane, 1987). In brief, these uncertainty intervals are calculated by a modified Tukey-Kramer procedure that assumes equal variance in both populations.

Figure S7, related to Figure 5. Schematics of drift calculation

(A) Schematic of an average firing field, in black, with axis overlaid. The region surrounding the firing field is given by the region between the black (circle with radius r) and dashed (circle with radius βr). (B) Schematic of drift calculation. The original field and the boundary of surrounding region are given in black, while the drifted field (shifted by value x_d) is schematized in gray. The red lines give example trajectories taken when calculating the probability of spiking during entry (or exit) given the angle of entry (or exit). (C) Schematic of increased variance calculation. Again, the original field and boundary of the surrounding region are given in black, while the expanded field (with radius $r + \delta$) and surrounding boundary is schematized in gray. The red lines give example trajectories taken when calculating the probability of spiking during entry (or exit) given the angle of entry (or exit). (D)-(E) Example trajectories taken with small (10 degrees, D) or large (180 degrees, E) angles between firing field entry and exit (10 degrees) at small (D-E, left) and large (D-E, right) amounts of drift. As in the previous panels, the black circle denotes the original field, while the solid gray circle denotes the drifted field. Green trajectory lines represent entry-to-exit trajectories where $\alpha\beta = -1$, where black trajectory lines represent entry-to-exit trajectories where $\alpha\beta = 1$. The average value of $\alpha\beta$ are given beneath each panel. Note that $\alpha\beta$ values are largest for small angles and large drift, while $\alpha\beta$ values are smallest for large angles and large drift. (F) Quantification of the value of $\alpha\beta$ over small and large angles for small drift magnitudes (drawn from left panels of (D) and (E)). (G) Quantification of the value of $\alpha\beta$ over small and large angles for large drift magnitudes (drawn from right panels of (D) and (E)).

Note that the decrease of $\alpha\beta$ from small to a large angle is more significant than in (F). This is meant to demonstrate the increased decrease of $\alpha\beta$ over angle as drift magnitude increases.

(H) Illustration of analysis for coherent drift. If grid fields do not drift in a single direction (top), the observed angle between these directions (as calculated from the spikes surrounding the firing field) may be large, even when the animal runs in a straight line through two fields. In contrast, if the grid fields drift in a single direction, the observed angle between these directions will be small (bottom). (I) The significantly negative slope reported in Figure 6D may reflect an asymmetric shift in high negative error values along the x-axis. That is, trajectories with stationary events will cause a selective shift of high error values along the x-axis. As a demonstration of this, we present spikes (illustrative, not derived from real data) from one neuron across two trajectories, one in red and one in green. Error relative to time since the last boundary encounter is plotted on the left. In the case of the green trajectory, a stationary event is noted with a green arrow. When the points that occur after this stationary event are shifted to zero along the x axis (right), the slope decreases.

Figure S8, related to Figure 7. Simulations of grid cells

Examples of 24 simulated grid cells with (A) or without (B) border cell input. In each case, four cells from three simulations were chosen to illustrate the heterogeneity of model output and robustness of the grid pattern with corrective border cell inputs.

Supplemental Experimental Procedures

Surgery and experimental data acquisition

Mice and their littermates (50:50 C57B6/129SvEv) were housed together until surgery, when mice ranged in age from 6 to 12 months (Eggink et al., 2014; Giocomo et al., 2011). For surgical implantation of the recording electrodes, mice were deeply anesthetized with isoflurane (induction chamber 3.0% with air flow at 1200 ml/min, reduced to 1% once the animal was secured in the stereotaxic apparatus) and a subcutaneous injection of buprenorphine (0.3 mg/ml). Two tetrodes (17 μ m) composed of polyimide-coated platinum iridium 90-10% wire were attached to the microdrive, cut flat and the electrode impedances reduced to ~200 k Ω at 1 kHz. The tetrode bundle was implanted in the left hemisphere, angled 4 – 8 degrees in the posterior direction in the sagittal plane, at AP .3 - .5 mm in front of the transverse sinus, 3.1 – 3.25 mm from the midline and .8 to 1.1 mm below the dura. The microdrive was secured to the skull using dental cement adhered to jeweler's screws, with one screw serving as the ground electrode.

After implantation, mice were housed in transparent plexiglass cages on a reverse light cycle, with testing occurring during the dark phase. Mice were placed in the box and allowed to explore untethered three days after surgery and one week after surgery (4 training sessions), mice were connected to the recording equipment via AC coupled unity-gain operation amplifiers and data collection began. Mice were placed in a recording box surrounded by curtains (1 x 1 m), with a white polarizing cue on the east wall, as defined in the manuscript, of the open field. Sessions lasted between 20 (n = 8 sessions) and 40 minutes (n = 258 sessions). Each mouse experienced the open field at least once per day and not more than twice per day (sessions separated by 3 hours). After each finished set of experiments, tetrodes were moved by 25 μ m until new well-separated cells were encountered (spike amplitudes exceeded two times the noise level). The floor of the test box was washed with soapy water between each trial. Before and after each session, the mice rested in their home cage.

Spikes were sorted with offline graphical cluster-cutting software (TINT software, Axona Ltd.). To ensure that each cell was only included in the analyses once, clusters and waveforms in TINT were compared between sessions. For 82% of sessions, tetrodes had moved at least 25 microns between recording sessions, with cells from the remaining 18% of sessions reflecting data from one out of two recording sessions at the same depth. The session in which the cell had the largest number of spikes was chosen as the representative data point. For grid cells, an average of 2 grid cells were recorded at any single anatomical depth (range = 1 to 7; with 45 out of 51 recording depths containing \leq 3 grid cells).

Electrodes were not moved after the final recording session. The mice were killed with an overdose of pentobarbital and transcardially perfused with 0.9% saline (wt/vol) followed by 4% formaldehyde (wt/vol). The brains were extracted and stored in 4% formaldehyde. At least 24 hours later, the brains were quickly frozen, cut in sagittal sections (30 μ m), mounted and stained with cresyl violet. The positions of the tips of the recording electrodes and measurements were determined from digital pictures of the brain sections made using AxioVision (LE Rel. 2.4).

Definition of grid cells

Rate maps were generated by dividing the 1 x 1 m open arena into 1.4 x 1.4 cm bins and calculating the ratio of spike number to bin dwell time. To classify grid cells, we first calculated a grid score by taking a circular sample of the autocorrelation and comparing it to rotated versions of the same circular sample (60° and 120° versus 30°, 90° and 150°). The minimum distance between elements in the first group (60°, 120°) and the second group (30°, 90°, 150°) was defined as the cell's grid score (Eggink et al., 2014; Langston et al., 2010; Sargolini et al., 2006). Grid cells were defined as neurons with a grid score in the 99th percentile (grid score > 0.41) of the distribution of scores generated from shuffled rate maps, where each spike was time-shifted along a trajectory by a fixed random amount (Langston et al., 2010). The same threshold was

used to define the population of rat grid cells analyzed. Grid spacing was calculated as the mean distance from the central peak in the spatial autocorrelation to the nearest 6 peaks. Additionally, to quantify the directional modulation of each cell, we calculated the mean Rayleigh vector length (referred to in text as head direction score or MVL) of the firing rate distribution across all head directions.

Identification of border cells and calculation of boundary region width

To calculate the boundary region width, we first identified border cells using a previously defined border score (Solstad et al., 2008):

$$\text{Border Score} = \frac{CM - DM}{CM + DM}$$

where CM is the proportion of high firing-rate bins located along one of the walls and DM is the normalized mean product of the firing rate and distance of a high firing-rate bin to the nearest wall. Border cells were identified as cells with a border score above 0.6 (Giocomo et al., 2011). Border cell rate maps were generated by dividing the open arena into 1.4 cm x 1.4 cm bins and calculating the firing rate in each bin (Figure S1A). Firing fields and the corresponding COM's were detected using the same field detection process and parameters for grid cell firing fields (Figure S1B). The width of the border cell firing field was calculated from fields with a COM less than 25 cm from the boundary of the environment and with a length of at least 10 cm. For each field, we determined the distance of each bin along the edge of the field to the nearest boundary (Figure S1C). The firing field width was then given as the mean of these distances. For each cell, a mean firing field width was then generated, which determined the mean field width over all border cells (Figure S1D).

Null Dataset

To approximate the probability that we would observe the slope magnitudes exhibited by SDM

vs time and SDM vs distance by chance, we constructed a null distribution of slopes by generating 500 non-error accumulating (null) data sets. Each null data set retains the same distribution of firing rates across positions and cells, and the same distribution of trajectories across animals, but there is no positional drift in the internal estimate of position. Each null data set is made up of 91 model grid cells. To construct each model grid cell in each null data set, we took the firing rate map (generated from the position and spike files) of one of the 91 grid cells and generated a new set of spikes for this cell by treating this firing rate map as a Poisson rate function for spiking as a function of locations determined by a new, randomly selected position file. More specifically, the probability of firing a spike during a given time interval ($T = 0.02$ s) is based on the firing rate at the locations along trajectories as dictated in the new position file. We were then able to determine the normalized distance of simulated Poisson spikes from the nearest center of mass (determined by the original rate map) along each trajectory as a function of time since leaving the border region. For each null data set, we were then able to compute the slope of the SDM versus time and SDM versus distance observed when considering trajectories > 60 s.

Null Animal Dataset

To quantify the significance of observing the effect across animals, we employed the null model technique to create “null” animals. For each null animal, we collected an amount of data comparable to the amount of data collected for each real animal listed in Figure S4 by matching the number of grid cells recorded within a single animal (4 to 26) and the number of trajectories 60 seconds or longer recorded per grid cell (1 to 7). More specifically, for each null animal, we randomly drew n number of grid cells (according to a normal distribution with mean and variance taken from the experimental data), with m trajectories per cell (randomly selected according to a uniform distribution). We then used the method above to generate spikes along each trajectory for each cell, and computed the SDM for each spike along each trajectory. We

then computed the significance of the slope for the resulting SDM versus time plot by running the same statistical procedures (bootstrapping, shuffling, and downsampling) that we ran on the real data to compute the three p-values associated with testing whether the slope of the SDM as a function of time is positive. We repeated this procedure to generate a set of three p-values associated with the three tests for 500 model animals. Finally, we computed the probability, across a randomly chosen animal, that all three p-values (bootstrapping, downsampling, shuffling) are < 0.05 . We find this probability to be 0.240. We also computed the probability that 2 of the tests (bootstrapping and shuffling) show significance in one animal. This probability is 0.300. Thus, using a binomial test, we found that the probability of seeing significance in all 3 tests in 4/6 animals is $p = 0.029$ and the probability of seeing significance in 2 of the tests in 5/6 animals is $p = 0.010$.

Field Asymmetry

To determine the degree of circularity for each field, we generated a circularity score by fitting each firing field with an ellipse (using `fit_ellipse` by Ohad Gal, retrieved in August 2014 from <http://www.mathworks.com/matlabcentral/fileexchange/3215-fit-ellipse>) and defining the score as the aspect ratio, or the minor axis divided by the major axis, of this ellipse. The most circular fields will return aspect ratios near unity.

Derivation of theoretical predictions for the coherent drift and increased variance models of error accumulation

In brief, we calculated the predicted functions $\alpha\beta(\theta)$ under the increased variance or drift hypothesis by first simulating a field that has either expanded or drifted, and finding the values of α and β for simulated trajectories that enter or exit the firing field at different angles. In the following description, we first explain how to find $\alpha\beta(\theta)$ for a “normal” (non-expanded, non-

drifted) field, and then we describe how to apply this analysis to fields that have expanded or drifted.

First, we considered a firing field whose firing rate at a particular location is approximated by a data-constrained Gaussian function, $F(\vec{x}) = A * \exp\left(\frac{-\vec{x}^2}{2r^2}\right)$, where the parameters $2r$ and A correspond to the mean firing field radius (9 cm, Figure S5A) and mean peak firing rate over all firing fields (17.9 Hz), respectively. The region surrounding the firing field is given as an annulus centered at the origin, with an inner radius of r and an outer radius of βr (Figure S7A). In this work, we take $\beta = 3/2$. As with the experimental data, we investigated the relationship between the occurrence of spikes during firing field entry and firing field exit by defining a step-wise function, $G(n) = \begin{cases} +1 & n > 0 \\ -1 & n = 0 \end{cases}$, that detects the presence or absence of spikes during entry (number of spikes during entry = n_e) or exit (number of spikes during exit = n_x). In terms of the variables mentioned in the main text, $G(n_e) = \alpha$ and $G(n_x) = \beta$. As in the experimental data, the value of α is determined from trajectories that travel from the outer to the inner ring (firing field entry), and the value of β is determined from trajectories traveled from the inner ring to outer ring (firing field exit), of the annulus surrounding the firing field (red lines in Figure S7B-C). For a given angle θ between firing field trajectory entry (θ_e) and exit (θ_x), we can compute $\alpha\beta$ by computing the probability of observing spikes on either entry or exit. That is, $\alpha\beta = P_e P_x + (1 - P_e)(1 - P_x) - ((1 - P_e)P_x + (1 - P_x)P_e)$, where $P_e = P(n_e > 0 | \theta_e, r, \beta)$ is the probability of observing at least one spike during firing field entry, and $P_x = P(n_x > 0 | \theta_x, r, \beta)$ is the probability of observing at least one spike during exit.

Analytically, the value of P_e is given by integration of the firing rate function F over the trajectory, or $P_e = A \int_E^X \exp\left(\frac{-\vec{x}^2}{2r^2}\right) dx$, where the start of the trajectory is given by the lower bound $E = (\beta r \cos(\theta_e), \beta r \sin(\theta_e))$ and the end of the trajectory is given by the upper bound $X = (r \cos(\theta_e), r \sin(\theta_e))$. P_x is defined similarly. Numerically, we computed P_e (and P_x) for every

trajectory by considering a trajectory that enters (or exits) the firing field with velocity = 15 cm/s (example trajectories given in Figure S7B-C; 15 cm/s was the average velocity over all trajectories). We then found the probability of observing at least one spike during this trajectory by dividing the trajectory into m bins (of time length T ; we use $m = 5$), and assuming Poisson spiking statistics to compute 1 minus the probability of observing 0 spikes in each bin, i.e. $P_e = 1 - e^{-(r_1 + \dots + r_m)T}$ where r_i is the firing rate of the i^{th} bin in the trajectory. In summary, computing the probability of observing at least one spike (or alternatively, no spikes) during a trajectory at a given angle allows us to compute the values of α and β . Further, we can perform this calculation for many trajectories at various angles, which will allow us to derive the mean values of the product $\alpha\beta$ across $\theta = \text{abs}(\theta_e - \theta_x)$.

We then employed this calculation to investigate firing field drift. We modeled a drifted field as a shifted Gaussian, or $F(\vec{x}) = A * \exp\left(\frac{-(\vec{x} - \vec{x}_d)^2}{2r^2}\right)$, where $\vec{x}_d = x_d * \vec{e}_{x_d}$ denotes the direction and magnitude of drift (Figure S7B). The magnitude of drift was calculated from the data, while the direction was modeled as (1,0) (due to circular symmetry, the chosen direction does not influence the results). As stated in the main text, the increase in mean spike distance from the nearest center of mass was calculated by multiplying the rate of burst distance increase (0.011 cm/s) by the time point (30 seconds or 120 seconds) at which we would like to examine the predicted function $\alpha\beta(\theta)$. We used these values (0.33 cm for 30 seconds and 1.32 cm for 120 seconds) to determine x_d at each time point by calculating the mean spike distance increase for various drift magnitudes for a Gaussian firing field (with parameters described above; $x_d = 2.17$ cm for 30 seconds and $x_d = 4.44$ cm for 120 seconds). Using this shifted firing field, we computed α and β for each trajectory by calculating the probability of observing at least one spike upon entry and exit and using the same process previously described, but with $P_e = A \int_E^X \exp\left(\frac{-(\vec{x} - \vec{x}_d)^2}{2r^2}\right) dx$, and $P_x = A \int_X^E \exp\left(\frac{-(\vec{x} - \vec{x}_d)^2}{2r^2}\right) dx$. Calculation of α and β for many

trajectories over many angles allowed us to find the mean value of the product $\alpha\beta$ across θ . We then binned accordingly to match the experimental results.

In the case of increased variance, we followed an identical procedure, but with an increasing radius of the firing field (increase given by δ) as opposed to a shifting firing field (Figure S7C). We found $\delta = 0.52$ cm after 30 seconds and $\delta = 2.1$ cm after 120 seconds. Additionally, in order to keep the area of the Gaussian constant, the value of $A = A' * \frac{r}{r+\delta}$, where $A = 17.9$ Hz. This assumption was made on the basis that we did not observe differences in the number of spikes at the beginning and end of trajectories, as the number of spikes that occur during the first and last 20 seconds of trajectories that are at least 60 seconds long differ by less 1% (11,827 spikes versus 11,725 spikes).

Shuffling analysis for drift

We shuffled the values of $\alpha\beta$ along the x-axis, and binned these values along the x-axis using bin widths of $\pi/3$. We then calculated the mean value of $\alpha\beta$ in each bin, and fit a first-order polynomial to these values. This procedure was carried out 10,000 times. The p-value represents the probability of observing a slope larger in magnitude than one observed by chance, which was calculated from the overlap between the original slope and the distribution of slopes generated from shuffled data. We use this shuffling procedure for the drift analysis as fitting a line to a discrete data set (containing only -1 and 1) using ordinary least squares results in large root-mean-square error, while fitting a line to the mean of each bin results in substantially lower root-mean-square error.

Implementation of attractor network model

Information on the attractor network model implementation is detailed in (Burak and Fiete, 2009); however, for purposes of completeness, we give the relative details in this section (code

available at available online at <http://clm.utexas.edu/fietelab/code.htm>). We model a network of 128^2 recurrently connected spiking grid cells with inherited direction preferences arranged on a 2-dimensional sheet. For our simulations, we assume the neural sheet has periodic boundary conditions, meaning that the neurons on the left edge of the sheet connect to the neurons on the right edge of the sheet, and the neurons on the top edge of the sheet connect to the neurons on the bottom edge of the sheet. Topologically, this makes the neural sheet a torus. Additionally, each neuron inhibits neighboring neurons (described in the equations below) such that in the presence of broad-field excitation, a grid pattern of activity emerges (as in Figure 7A). Single grid cell responses are then generated when the velocity of the animal is coupled to the movement of the neural sheet activity pattern. In MEC, this coupling of pattern movement to animal movement may be accomplished by input from head-direction cells or conjunctive grid x head-direction cells (Burak and Fiete, 2009; Fuhs and Touretzky, 2006; Sargolini et al., 2006). As in Burak and Fiete 2009, this input in our simulations is captured by an inherited grid cell head-direction preference (N, S, E, or W).

The differential equation governing the synaptic activation, s_i , of grid cell i is given by:

$$\tau \frac{ds_i}{dt} + s_i = f \left(\sum_j H_{ij} s_j + \sum_d W_{id} B_d + C_i \right)$$

The neural transfer function $f(y) = \begin{cases} y, & y > 0 \\ 0, & y \leq 0 \end{cases}$ takes the total input to the neuron, and returns synaptic activity for that neuron. The parameter H_{ij} denotes the synaptic weight from cell j to cell i , and is given by $H_{ij} = H_0(x_i - x_j - l\hat{e}_{\theta_j})$ with weight matrix $H_0(x) = ae^{-\gamma|x|^2} - e^{-\beta|x|^2}$.

This weight matrix is centered on $x - l\hat{e}_{\theta_j}$, where θ_j denotes the direction preference of that cell. Following (Burak and Fiete, 2009), we use $a = 1$, $\gamma = 1.05 * \beta$, and $\beta = 3/13^2$. Additionally, the parameter $\tau = 30$ ms denotes the neural integration time constant (Garden et al., 2008), while the time step of numerical integration is $dt = 3$ ms. C_i gives the feed-forward input to grid cell i ,

where $C_i = \alpha \hat{e}_{\theta_i} \cdot v$ is the product of a scaling term $\alpha = 1$, the direction of the animal as denoted by the unit vector \hat{e}_{θ_i} pointing in the direction θ_i , and velocity v ($\max(v) = 12$ cm/s).

Lastly, B_d gives the activity of border cell d , which is only when the animal is physically located in region R_d , i.e. $B_d = \begin{cases} c, & \vec{x} \in R_d \\ 0, & \vec{x} \notin R_d \end{cases}$. For the simulations presented, we take $c = 1$, and R_d to be a region (with width = 1 cm) along a particular border (either the N, S, E, or W border). W_{id} denotes the synaptic weight from border cell d to grid cell i . This value is proportional to the superposition of the grid cell's activity when the animal is at different points in the region R_d , or $W_{id} = \frac{1}{N} \int_{R_d} r_i(\vec{x}) d\vec{x}$ with $N = 20$. Although this model uses only simplified border cells that are associated with one border and have relatively narrow firing fields, we expect that these findings will generalize to cells with spatially sparse firing patterns anchored to a particular environmental landmark, including border cells with a larger border width and border cells that code for corners of a rectangular arena.

To model individual grid spikes, we followed (Burak and Fiete, 2009) in simulating Poisson spiking. At each time step (every 3 ms), each neuron spikes with a probability given by the current synaptic activation. If a neuron does spike at a given time step, synaptic activation for that neuron is incremented by 1. Otherwise, this variable exhibits exponential decay. This neural noise, in combination with the fact that there are finite neurons in this network, underlie the observed translational drift in the activity pattern.

Supplemental References

Burak, Y., and Fiete, I.R. (2009). Accurate path integration in continuous attractor network models of grid cells. *PLoS Comput Biol* 5, e1000291.

Eggink, H., Mertens, P., Storm, I., and Giocomo, L.M. (2014). HCN1 independent grid cell phase precession in mice. *Hippocampus* 24, 249-256.

Fuhs, M.C., and Touretzky, D.S. (2006). A spin glass model of path integration in rat medial entorhinal cortex. *J Neurosci* 26, 4266-4276.

Garden, D.L., Dodson, P.D., O'Donnell, C., White, M.D., and Nolan, M.F. (2008). Tuning of synaptic integration in the medial entorhinal cortex to the organization of grid cell firing fields. *Neuron* 60, 875-889.

Giocomo, L.M., Hussaini, S.A., Zheng, F., Kandel, E.R., Moser, M.B., and Moser, E.I. (2011). Grid cells use HCN1 channels for spatial scaling. *Cell* 147, 1159-1170.

Hochberg, Y., and Tamhane, A.C. (1987). *Multiple comparison procedures* (New York, NY, USA: John Wiley & Sons, Inc.).

Langston, R.F., Ainge, J.A., Couey, J.J., Canto, C.B., Bjerknes, T.L., Witter, M.P., Moser, E.I., and Moser, M.B. (2010). Development of the spatial representation system in the rat. *Science* 328, 1576-1580.

Sargolini, F., Fyhn, M., Hafting, T., McNaughton, B.L., Witter, M.P., Moser, M.B., and Moser, E.I. (2006). Conjunctive representation of position, direction, and velocity in entorhinal cortex. *Science* 312, 758-762.

Solstad, T., Boccara, C.N., Kropff, E., Moser, M.B., and Moser, E.I. (2008). Representation of geometric borders in the entorhinal cortex. *Science* 322, 1865-1868.

Wilber, A.A., Clark, B.J., Forster, T.C., Tatsuno, M., and McNaughton, B.L. (2014). Interaction of egocentric and world-centered reference frames in the rat posterior parietal cortex. *J Neurosci* 34, 5431-5446.